The Cryosphere, 20, 5025–5039, 2026
https://doi.org/10.5194/tc-20-5025-2026

The Cryosphere Open Access EGU

GPR-derived ice thickness of the temperate Hintereisferner glacier (Austrian Alps): evaluation of thickness models

Lelde Švinka, Kristaps Lamsters, Jānis Karušs, Pēteris Džeriņš, and Jurijs Ješkins

Faculty of Science and Technology, University of Latvia, Jelgavas Street 1, 1004, Riga, Latvia

Correspondence: Lelde Švinka (lelde.svinka@lu.lv)

Received: 10 February 2026 – Discussion started: 5 March 2026
Revised: 2 July 2026 – Accepted: 26 August 2026 – Published: 7 September 2026

Abstract. Alpine glaciers are retreating rapidly and have a potential for near complete ice loss at the end of the 21st century thus accurate glacier evolution models are crucial for predicting the magnitude and rate of future glacier changes. Without reliable ice thickness assessments, such models lack credibility and cannot be validated, thus here we evaluate several ice thickness models and present new ground-penetrating radar (GPR) ice-thickness measurements of the Hintereisferner – a temperate glacier located in the Ötztal Alps, Austria, which despite being one of 60 WGMS reference glaciers lacks up-to date measured ice thickness data.

The GPR data is characterized by strong signal scattering, typical for temperate ice with high water content, however the glacier bed is detectable in most profiles. GPR measurements reveal a maximum ice thickness of ~ 162 m along the central flowline and a mean thickness of 81.1 ± 37.4 m (± 1 standard deviation) across the surveyed area. We further select three widely used, open-source ice-thickness models, GlabTop2, OGGM, and Millan et al. (2022), and compare their output to the GPR-derived ice thickness. All models systematically overestimate ice thickness across the surveyed area, with mean positive biases ($\pm 1\sigma$) of 41 ± 36 m for GlabTop2, 49 ± 38 m for OGGM, and 46 ± 57 m for Millan et al. (2022), while only minor and localized underestimation occurs along the central flowline. These results highlight the limitations of predominantly geometry-based and velocity-informed modelling approaches when applied to small, temperate valley glaciers, where ice rheology and basal conditions may have greater influence on the resulting thickness than these algorithms allow.

1 Introduction

Mountain glaciers have been retreating since the mid-19th century, with the rate of mass loss accelerating since the 1980s, including alpine glaciers (Hugonnet et al., 2021; The GlaMBIE Team et al., 2025; Zemp et al., 2019). Alpine glacier dynamics and their ongoing sensitivity to climate change are strongly influenced by glacier elevation, topography, and overall geometry (Fischer, 2010; Santin et al., 2019). Glacier inventories for the European Alps and Austria specifically are well developed (Fischer et al., 2015; Fischer and Kuhn, 2013), while direct measurements of glacier thickness generally remain sparse in both space (often only point-wise measurements are available) and time with some exceptions for Austrian glaciers. Since ice thickness is a key parameter for estimating glacier volume and future evolution, reliable ice thickness maps are essential for calibrating ice-flow models, which in turn are used to predict glacier evolution under different emission scenarios.

To address this data gap, numerous modelling approaches have been developed to estimate glacier thickness and volume, mainly by utilizing information about glacier surface characteristics such as shape, slope, velocity or mass-balance, to invert for ice thickness (Farinotti et al., 2009; Frey et al., 2014; Maussion et al., 2019; Millan et al., 2022; Raper et al., 2000). Further global or Alpine glacier evolution modelling (e.g. Cook et al., 2023; Hartl et al., 2025; Shafeeque et al., 2026; Van Tricht et al., 2026; Zekollari et al., 2024) relies on the accuracy of these ice thickness models. However, despite the broad applicability of thickness models, some studies have shown that great discrepancies can arise between modelled and measured ice thickness at a local scale, particularly for relatively small valley glaciers, where simplified

Published by Copernicus Publications on behalf of the European Geosciences Union.

assumptions and poorly constrained parameters can lead to large spatial and systematic errors (Forte et al., 2025; Lamsters et al., 2024; Švinka et al., 2025).

Thus, field-based studies remain vitally important, including datasets that are collected for prolonged periods, and can provide ice volume change estimates and help calibrate modelling efforts. As a notable case and an example is the Marmolada glacier in the Dolomites, where repeated ground-penetrating radar (GPR) surveys conducted in 2004 and 2015 showed the reduction of the ice volume by $\sim 30\,\%$ and suggested possible glacier disappearance by mid-century (Santin et al., 2019). Alpine glacier retreat is accelerating as seen in numerous studies, for example, data from geodetic mass balance of glaciers in Ötztal Alps revealed that from 1969 to 2006 they experienced mean annual ice volume loss increase by $\sim 50\,\%$ and thickness reduction by more than $\sim 70\,\%$ (Abermann et al., 2009). Galos et al. (2025) reported 41 % reduction of glacierized area in South Tyrol between 1997 and 2023 emphasizing the extremely rapid glacier retreat during the last decades. Even more – since 1973, more than 1000 glaciers have completely vanished in the Swiss Alps (Linsbauer et al., 2025) highlighting the great sensitivity of such small Alpine glaciers. Projections suggest that this trend will continue, with up to two thirds of Alpine glacier volume lost by the end of the 21st century (vs. 2017) under RCP2.6 scenario and near-complete deglaciation under RCP8.5 (Hartl et al., 2025; Van Tricht et al., 2026; Zekollari et al., 2019).

In this study, we present new GPR-derived ice thickness measurements for Hintereisferner (HEF), one of 60 reference glaciers of the World Glacier Monitoring Service (WGMS, 2026), obtained using a low-frequency, hand-held radar system. Our objectives are to (1) provide an updated ice thickness dataset for this WGMS reference glacier, (2) assess the spatial variability of bedrock detectability under temperate conditions, and (3) evaluate the performance of commonly used ice thickness models against direct measurements.

2 Study area

Hintereisferner is located in Rofental, Ötztal Alps, Austria (Fig. 1) covered an area of $5.17\,\mathrm{km}^2$ in 2022. It descends from 3.7 to 2.5 km a.s.l. Long-term direct mass balance observations of HEF demonstrate that it has been losing mass since mid-20th century, with continuous negative balances since the mid-1980s and surface lowering of up to $\sim 160\,\mathrm{m}$ at the glacier tongue by the early 2000s (Fischer, 2010; Fischer et al., 2012). Further reanalyses (Klug et al., 2018) show glaciological mass balances for 2001–2011 ranging from -0.624 ± 0.21 m w.e. (2001/02) to -1.813 ± 0.21 m w.e. (2006/07), and a corrected geodetic mass balance totalling -13.41 ± 0.29 m w.e. over the same decade, with annual values between -0.654 ± 0.06 m w.e. (2003/04) to -2.713 ± 0.18 m w.e. (2002/03).

Flow velocity, length, and thickness change observations at HEF span more than 150 years (Stocker-Waldhuber et al., 2024; Strasser et al., 2018), making it one of the best-documented Alpine glaciers. HEF is the key glaciological study site serving as an open-air laboratory and has been used as a test bed for various glaciological and meteorological applications (Mott et al., 2020; Nicholson et al., 2025; Strasser et al., 2018; Voordendag et al., 2023a, b). The long-time series of glaciological and meteorological observations have been also used to develop and validate glacier models (e.g. Maussion et al., 2019; Raper et al., 2000).

Despite this long research history, direct measurements of ice thickness remain limited. The most comprehensive GPR-based thickness dataset dates back to 2001 and consists of 145 point measurements, indicating a maximum ice thickness of 242 ± 13 m (Fischer and Kuhn, 2013). Subsequent GPR surveys have focused primarily on snow thickness rather than ice thickness (Helfricht et al., 2014). As a result, no up-to-date, spatially detailed ice thickness dataset exists for HEF, limiting modelling and other studies which may benefit of ice thickness data for this reference glacier, including studies arising from the availability of a permanent long-range terrestrial laser scanning system since 2016 (Chambers et al., 2021; Voordendag et al., 2023b).

3 Data and Methods

We conducted fieldwork on HEF in the Ötztal Alps from 2–7 August 2023. We collected glacier thickness and internal structure data using GPR and recorded all profiles on a snow-free glacier surface (Fig. A1). We used a GNSS receiver (Emlid Reach RS2) to ensure precise positioning of the GPR profiles. A digital surface model (DSM) was obtained from an airborne laser scanning (ALS) campaign conducted on 23 September 2022, and provided by Rainer Prinz (Department of Atmospheric and Cryospheric Sciences, University of Innsbruck, Austria). The glacier outline was derived from Pléiades satellite images that were acquired on 21 August 2022 (Pléiades © CNES 2022, Distribution Airbus D&S).

3.1 GPR survey

GPR is a widely used geophysical method for glacier thickness and internal structure investigations (Bogorodsky et al., 2012; Karušs et al., 2019, 2022; Lamsters et al., 2020a, b, 2024; Navarro and Eisen, 2009; Pellikka and Rees, 2009; Sevestre et al., 2015). The main factors influencing GPR performance in glacial environments include the specifications of a GPR system (e.g. frequency, power) and the physical properties of ice, such as density and water content, which affect dielectric permittivity and signal attenuation (Ogier et al., 2023; Schroeder et al., 2020; Watts and England, 1976). Temperate Alpine glaciers commonly contain liquid

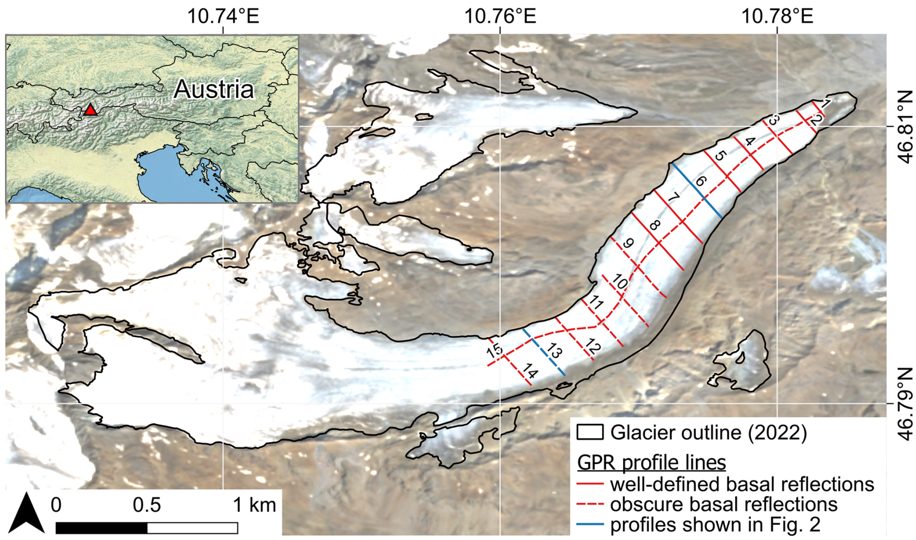

Figure 1. Hintereisferner glacier – profile location. Copernicus Sentinel-2 composite image (T32TPS_20230819T101609) at the background.

water, resulting in strong radar signal attenuation and limited bedrock detectability. As shown by Ogier et al. (2023), liquid water contents as low as ~ 0.2 % (typical for Alpine glaciers) can significantly impede bed detection for ice thicknesses exceeding ~ 100 m.

In this study, we conducted a GPR survey using a terrestrial Zond-xLF GPR system manufactured by Radar Systems, Inc. Given the temperate nature of Alpine glaciers, maximizing penetration depth was a priority, therefore, we used an antenna with the lowest possible frequency (38 MHz) compatible with our radar system, as higher-frequency signals are more susceptible to absorption in temperate ice conditions (Murray et al., 2007; Ogier et al., 2023). We selected a time window of 2560 ns with a range per sample of 1250 ps for shallower parts and 2500 ps for deeper sections, and 2048 samples per trace, which allowed for a theoretical maximum penetration depth of ~ 210 m, assuming a dielectric permittivity of 3.2 (cold-ice value, Church et al., 2020; Robin, 1975; Rutishauser et al., 2016).

We oriented the GPR profiles mainly transverse to the ice flow direction with 200 m spacing in between to optimize data collection within the available timeframe and to gather enough data points for subglacial valley mapping. Transverse profiles were preferred over along-flow profiles for two reasons: they better characterise the cross-sectional shape of the subglacial valley, and they maximise the chance of crossing englacial conduits oriented parallel to flow, producing characteristic hyperbolic reflections that allow these features to be identified (Jol, 2008). Additionally, we recorded one profile parallel to the ice flow direction (Fig. 1). Prior to the GPR survey, we created a waypoint plan with 50 m step size to ensure we could precisely and easily follow our predetermined profile layout on the glacier. During the survey, we used a Garmin Montana 610 GNSS receiver to navigate along the waypoints, while Emlid Reach RS2 GNSS receivers provided precise positioning of the GPR profiles.

We processed the gathered GPR data using Prism 2.7 software. Our processing workflow included the application of manually adjusted time-dependent signal gain function and Ormsby band-pass filter with a low frequency cut-off at 20 MHz and a high frequency cut-off at 70 MHz. We applied topographical corrections using the elevation data from the DSM. During data interpretation, we extracted the two-way travel time (TWTT) for basal reflections from each GPR-profile along its entire length or where visible, picking individual travel-time measurements approximately every 10 m along the profile. Two GPR specialists independently interpreted the bed reflection across the full profile set. As the two interpretations were generally consistent for profiles with clear basal reflections but diverged in sections with weaker or ambiguous reflections, we retained the complete set of picks from the more conservative interpreter throughout, to ensure picking uncertainty remained consistent and comparable across all profiles. Due to intense internal signal scattering, we could not apply a hyperbola matching function for GPR signal velocity determination, and an equipment malfunction prevented us from conducting a common-midpoint survey. Consequently, we set the GPR propagation speed to $0.168\,\mathrm{m\,ns^{-1}}$, which corresponds to a dielectric permittivity of 3.2 – the typical value for cold ice conditions (Robin, 1975). Our assumed value of $0.168\,\mathrm{m\,ns^{-1}}$ is consistent with other GPR studies on temperate Alpine glaciers, e.g. Church et al. (2020) and Rutishauser et al. (2016), who used 0.1689 and $0.168\,\mathrm{m\,ns^{-1}}$, respectively, for Swiss Alpine glaciers. The implications of this assumption are discussed in Sect. 3.3.

3.2 Thickness data and modelling

We interpolated glacier thickness point data derived from the GPR survey using cubic interpolation algorithms. We chose cubic interpolation as a compromise between more simplistic methods (e.g. inverse-distance weighting) and more geostatistical approaches (e.g. kriging), providing a relatively smooth thickness field and honouring the measured values. To prevent unrealistic values along the glacier margins, we assigned a uniform boundary thickness of 0.1 m to points along the glacier outline. In addition to the GPR-derived ice thickness measurements, we evaluated three widely-used, open-source ice thickness models: GlabTop2 (Frey et al., 2014), OGGM v1.6.2. (Maussion et al., 2019), and Millan et al. (2022) global model. These models differ in implementation algorithms and input data, although they ultimately derive ice thickness from glacier surface geometry and simplified ice flow assumptions.

The GlabTop2 model calculates ice thickness from surface slope using a shear-stress based approach, while the OGGM model inverts ice thickness along the central flowline based on mass conservation laws, calibrated against WGMS direct glaciological mass balance observations for HEF. The Millan et al. (2022) model inverts ice thickness from satellite-derived glacier surface velocities acquired in years 2017–2018, utilizing regionally calibrated ice rheology parameters and geometry-based regularization.

For the GlabTop2 and OGGM models, we used open-source Python implementations with glacier outline and digital elevation model (DEM) as input, applying default parameters throughout for both models – including the OGGM ice dynamics parameters (inversion_glen_a $= 2.4 \times 10^{-24}\,\mathrm{s^{-1}\,Pa^{-3}}$, inversion_fs $= 0$). For the Millan et al. (2022) ice thickness was extracted directly from the published dataset. However, since Millan et al. (2022) dataset represents glacier conditions for the 2017–2018 period, for the accuracy assessment, the thickness values were adjusted to account for the temporal offset to our GPR data acquisition date of August 2023. We derived the correction from elevation-band cumulative mass balances reported by the WGMS for the 2018–2023 period, converted to surface elevation change assuming an ice density of $900\,\mathrm{kg\,m^{-3}}$. We applied this correction only for the statistical comparison at GPR measurement points, while all visual materials (maps, difference maps, and scatterplot) retain the original 2017–2018 geometry.

All scripts used for model setup and execution are provided in the Zenodo repository (Švinka et al., 2026) to ensure full reproducibility. All generated maps are in WGS84/UTM zone 32N coordinate system and ellipsoidal height.

3.3 Uncertainty and accuracy assessment

We did all uncertainty and accuracy calculations based on the measured GPR point data ($n = 1313$), while we used the interpolated thickness and bedrock maps solely for visualization purposes to avoid introducing interpolation artefacts.

In our survey GPR velocity could not be measured in-situ, therefore a standard cold-ice (0 % water content) velocity value of $0.168\,\mathrm{m\,ns^{-1}}$ was applied, introducing a systematic bias in our GPR-derived thickness values. Given that Hintereisferner is classified as a temperate glacier and some level of internal scattering is visible in all the GPR-profiles, possibly indicating high water saturation, the true EM velocity likely is lower, as it decreases with increasing liquid-water content (Bradford and Harper, 2005; Delf et al., 2022; Murray et al., 2000, 2007; Navarro and Eisen, 2009). This would result in shallower true ice thickness than calculated using the cold-ice value of $0.168\,\mathrm{m\,ns^{-1}}$.

To bound the potential effect of water content, we compare our assumed cold-ice velocity against the temperate Falljökull glacier, Iceland Murray et al. (2000), where a mean EM velocity of $0.156\,\mathrm{m\,ns^{-1}}$ was measured. This value represents an exceptionally water-saturated case that provides a conservative lower bound on velocity. The intense englacial scattering present in our GPR profiles suggests HEF might also contain significant water content, justifying inclusion of this lower bound on EM velocity. Using the Falljökull value, our assumed value would correspond to +7 % systematic overestimation in ice thickness. In addition, uncertainty in the resolution of bed-reflection picking introduces a locally variable random error of $\pm\lambda/2$, which for our 38 MHz antenna and EM velocity of $0.168\,\mathrm{m\,ns^{-1}}$ equals ± 2.2 m ($\sim$ 2 %–3 % of the mean ice thickness). Considering both sources of uncertainty – the dominant positive velocity bias and the smaller, spatially variable picking error – the worst-case overestimation of ice thickness is likely up to $\sim$ 10 %, whereas the typical uncertainty represents a positive bias of only a few percent.

To evaluate the accuracy of modelled ice thickness data, we compared the modelled and measured (GPR-derived) values using mean error or bias (ME), relative error (RE), and root-mean-square error (RMSE), defined as:

$$\mathrm{ME} = \frac{1}{n}\sum\nolimits_{i=1}^{n}(h_{\mathrm{mod},i} - h_{\mathrm{GPR},i}), \quad (1)$$

$$\mathrm{RE} = \frac{h_{\mathrm{mod}} - h_{\mathrm{GPR}}}{h_{\mathrm{GPR}}} \cdot 100\,\%, \quad (2)$$

$$\mathrm{RMSE} = \sqrt{\frac{1}{n}\sum\nolimits_{i=1}^{n}(h_{\mathrm{mod},i} - h_{\mathrm{GPR},i})^2}, \quad (3)$$

where h_{mod} and h_{GPR} are the modelled and measured ice thickness, respectively. These metrics were chosen to summarize the direction and magnitude of deviation from the GPR measurements in a simple and interpretable way.

4 Results

During fieldwork, 15 GPR-profiles were collected, spanning approximately 8.5 km and covering $\sim 1.3\,\mathrm{km^2}$ of the lower tongue of HEF. GPR signal quality varied spatially, with strong and well-defined basal reflections (Fig. 2a) in the lower ablation area (Fig. 1, profiles 1–8) and increasingly obscured reflections (Fig. 2b) towards higher elevations along the centre flowline (Fig. 1, profiles 9–15). Notably, in the GPR-profile recorded along the ice flow direction (Fig. 1, profile 15), the glacier bed was obscured in several sections where it was visible in the transverse profiles. We show a representative profile for each case in Fig. 2: a clearly visible glacier bed (Fig. 2a, profile 6) and an obscured bed (Fig. 2b and c, profile 13), where Fig. 2c shows the location of the interpreted bed picks. Bed picks for all 15 profiles that we manually identified from the GPR data, are provided in our data repository (Švinka et al., 2026). Except for reflections from the glacier bed and vertically stacked hyperbolae attributed to supraglacial channels and crevasses, GPR-profiles are characterized by intense EM wave scattering (Fig. 2). Such scattering according to numerous studies of polythermal and temperate glaciers in Svalbard (Karušs et al., 2022; Sevestre et al., 2015), Iceland (Lamsters et al., 2020b; Murray et al., 2000), Sweden (Gusmeroli et al., 2012; Rippin et al., 2011), Greenland (Forte et al., 2025; Lamsters et al., 2024) and Alps (Binder et al., 2009; Rutishauser et al., 2016; Santin et al., 2019) is clearly an indication of temperate ice with high water content. There is basically no transparent (scatter-free) ice except for the very topmost part of few profiles at the highest elevation (Fig. 2b, label 4) that may be related to a piezometric surface, above which the water content decreases sharply as noted by Murray et al. (2000), Lamsters et al. (2020b) and demonstrated by a combination of GPR measurements and borehole data by Jania et al. (1996). Also, Bradford and Harper (2005) found a similar distinct boundary (upper low-water content/lower high-water content layer) in temperate glacier in Alaska, which specifically coincided with the average piezometric surface measured in boreholes. Therefore, the lack of EM wave scattering suggests that the transparent upper ice is not cold ice but reflects the boundary between high and low water content within temperate ice due to the absence of water that could trigger such scattering. Reflections labelled "2" in Fig. 2a we interpret as hyperbolic diffraction patterns from supraglacial channels and crevasses – point or line scatterers near the glacier surface. These features are not persistent across all profiles, consistent with the spatially variable distribution of surface crevassing and channelling observed in the field and were not considered further in the bed interpretation.

4.1 Subglacial topography and ice thickness

The interpolated ice thickness map (Fig. 3c) reveals a distinct subglacial trough aligned with the glacier flow. The maximum detected ice thickness of ~ 160 m occurs along the central flowline at an elevation of ~ 2870 m, while ice gradually thins toward both the margins and the terminus. The mean ice thickness of the surveyed area is 81.1 ± 37.4 m (± 1 standard deviation (σ)). The derived bedrock topography (Fig. 3d) reveals a U-shaped valley with bedrock elevations ranging from ~ 2540 to 2940 m. The subglacial valley is slightly asymmetrical with the NW slope being steeper, while at the upper reaches of the study area it is the opposite. The longitudinal glacier cross-section (Fig. 3d, inset), extracted along the central flowline from the interpolated bedrock elevation map, indicates a down-glacier gradient with an evident rise in bedrock topography at around 1.8 km from the terminus. This coincides with an apparent local thinning in the interpolated thickness map (Fig. 3c) and a steeper slope visible in the DSM (Fig. 3a). We also found the slightly undulating bed up-glacier and more notable overdeepening down-glacier. However, the glacier bed is not fully identifiable in the GPR profiles starting from the bedrock rise, visible as discontinuities in the GPR thickness point-measurements (Fig. 3b) and corresponding to the boundary between well-defined and obscure basal reflections (Figs. 1 and 3c). Therefore, the apparent ice thinning and morphology of the rise should be interpreted with caution. We do not further expand the probable connection and causes between the bedrock rise and bedrock signal weakening up-glacier due to the lack of other evidence and to avoid overinterpretation. But it is worth noting that the bedrock rise and overdeepening has been reported in other studies (Förtsch and Vidal, 1956; Span et al., 2005). Overall, the spatial pattern of interpolated thickness and derived bedrock topography is best represented in the lower half of the survey area, where bed visibility was highest, and the uncertainty increases toward the upper half of the survey area, where interpolation relied on fewer measurement points.

4.2 Ice thickness models

The modelled ice thickness distributions from GlabTop2, OGGM and Millan et al. (2022) represent the entire glaciated area but were clipped to match our GPR-surveyed region. All three models generally reproduce similar geometries, with maximum thickness in the lower half of the glacier, coinciding with the GPR-surveyed area (Fig. 4a, c, and e). The maximum modelled ice thickness is 167 m for GlabTop2, 246 m for OGGM, and 247 m for Millan et al. (2022).

The thickness difference maps between modelled and GPR-interpolated thickness (Fig. 4b, d, and f) reveal a consistent pattern of overestimation, particularly along the glacier margins. Maximum positive deviations range from ~ 146 m for GlabTop2, 173 m for OGGM, and 207 m for Millan et al. (2022). Negative deviations are comparatively small, reaching -27 m for GlabTop2, -10 m for OGGM and -68 m for Millan et al. (2022). Ice thickness tends to be slightly underestimated along the centre flowline for the GlabTop2 and Millan models, although these values are several times smaller than the overestimations. The potential influence of the DSM temporal offset on these patterns is discussed in Sect. 5.2.

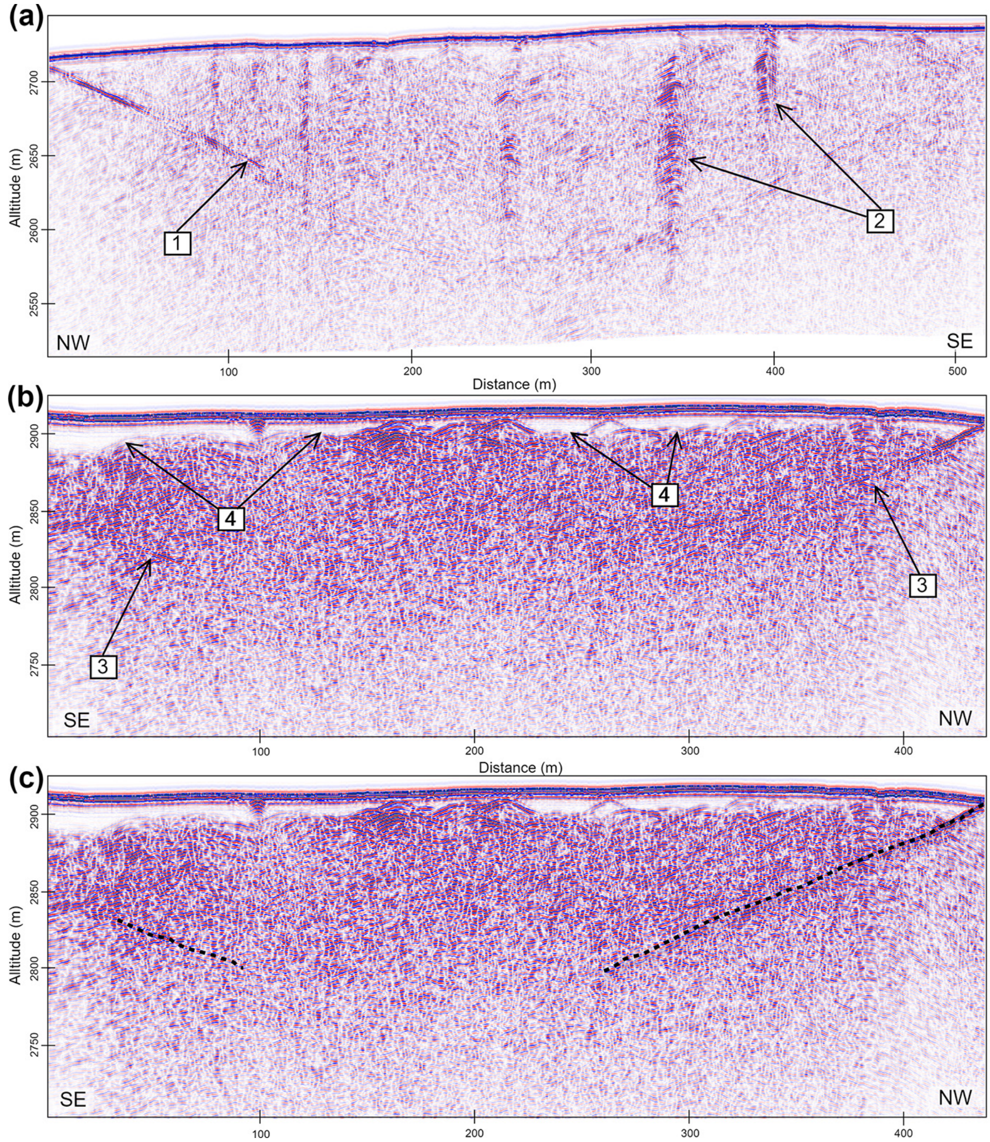

Figure 2. Examples of GPR profiles. **(a)** Profile 6, **(b)** Profile 13 without bedrock picks, and **(c)** Profile 13 with picked bedrock (dashed black line) digitised for illustrative purposes (see Fig. 1 for locations). Numbers indicate: 1 – clearly visible glacier bed; 2 – reflections from supraglacial channels and crevasses; 3 – partially visible glacier bed; 4 – boundary between low-scattering upper ice and high-scattering lower ice, interpreted as the piezometric surface.

The mean modelled ice thickness and corresponding error statistics for all three models are summarised in Table 1. These results reveal a consistent positive bias across all three models, reflecting a general pattern of ice thickness overestimation, also visible in measured vs. modelled ice thickness scatterplots (Fig. 5). Here, GlabTop2 shows a relatively narrow range of modelled thickness, mostly between 100 and 150 m, with a clear horizontal banding pattern aligned with elevation. This indicates that GlabTop2 tends to produce spatially uniform thickness distribution, and fails to represent the local extremes, as revealed by GPR data. In contrast, OGGM and Millan et al. (2022) show a wider spread of modelled values, although both, like GlabTop2, still substantially overestimate ice thickness across the survey area and present some degree of elevation banding as well. The largest spatial variability in model bias occurs for Millan et al. (2022), whose bias standard deviation (±57.0 m) exceeds its mean bias (Table 1).

As an additional metric, total ice volume for the surveyed area is 0.103 km^3 for GPR, 0.161 km^3 for GlabTop2 (RE 56.7 %), 0.194 km^3 for OGGM (RE 89.0 %), and 0.175 km^3 for Millan et al. (2022), without adjusting for temporal offset (RE 70.9 %). These volume estimates should be interpreted with caution, as they were calculated from each model's

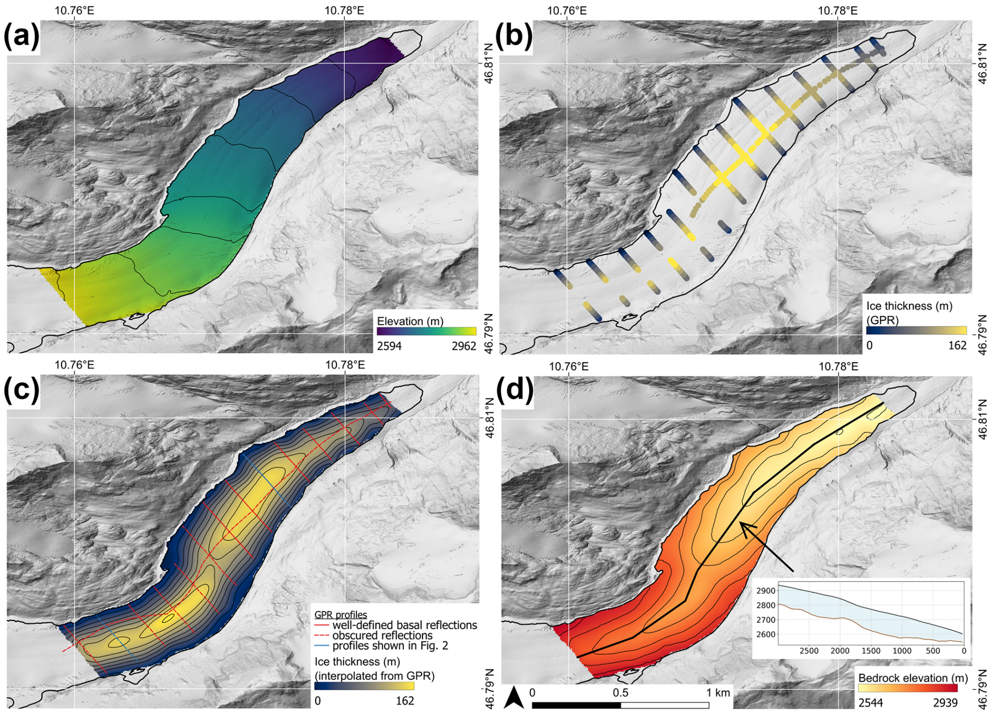

Figure 3. (a) Surface elevation from the 2022 DSM (contour interval 50 m). **(b)** Measured GPR ice thickness points. **(c)** Interpolated ice thickness distribution (contour interval 20 m). **(d)** Bedrock elevation (contour interval 50 m) derived from interpolated GPR data with longitudinal profile along the central flowline (inset). Background hillshaded DEM data source: basemap.at (basemap.at, 2024).

Table 1. Statistical comparison between GPR-derived and modelled ice thickness values, based on 1313 GPR measurement points.

Method	$\overline{h} \pm \sigma$ (m)	$\mathrm{RE}_{\overline{h}}$ (%)	ME $\pm\, \sigma$ (m)	RMSE (m)
GPR	81.1 ± 37.4	–	–	–
GlabTop2	121.6 ± 19.9	50.0	40.6 ± 35.6	53.9
OGGM	131.5 ± 54.8	62.3	48.6 ± 37.5	61.4
Millan et al., 2022 (adjusted)	127.5 ± 44.9	57.2	46.0 ± 57.0	73.2

native raster resolution, which differs substantially between models (particularly for Millan et al., 2022), introducing additional uncertainty unrelated to model performance itself.

5 Discussion

5.1 Ice thickness model performance and spatial patterns

The comparison between GPR-derived ice thickness and the three modelling approaches used in this study reveals a systematic ice thickness overestimation across the surveyed area of HEF, with broadly comparable mean error magnitudes across all three models (Table 1). The models differ primarily in the spatial distribution of this bias. The OGGM model best reproduces the overall geometry of the GPR-derived thickness field, with thickness maximised along the central flowline and thinning towards the margins (Figs. 4c and 3c). This likely reflects the valley-confined geometry of HEF, for which the flowline-based algorithm and enforced flux continuity of this model are particularly well suited (Maussion et al., 2019). However, this correct geometric representation does not translate into accurate thickness magnitudes: OGGM shows the largest mean bias of the three models (Table 1), indicating that reproducing the correct spatial pattern alone is insufficient to constrain absolute ice thickness. GlabTop2's spatially uniform bias field, by contrast, reflects a documented sensitivity to slope and DEM quality, alongside the relative robustness of OGGM to these same factors (Chen et al., 2022; Pelto et al., 2020). Millan et al. (2022) shows a qualitatively similar spatial pattern to GlabTop2 – underestimating thickness in the central trough while overestimating near the margins – but at a substantially larger magnitude: the bias standard deviation for Millan et al. (2022) (±57.0 m) is nearly three times that of GlabTop2 (±19.9 m; Table 1), despite comparable mean bias (46.0 m

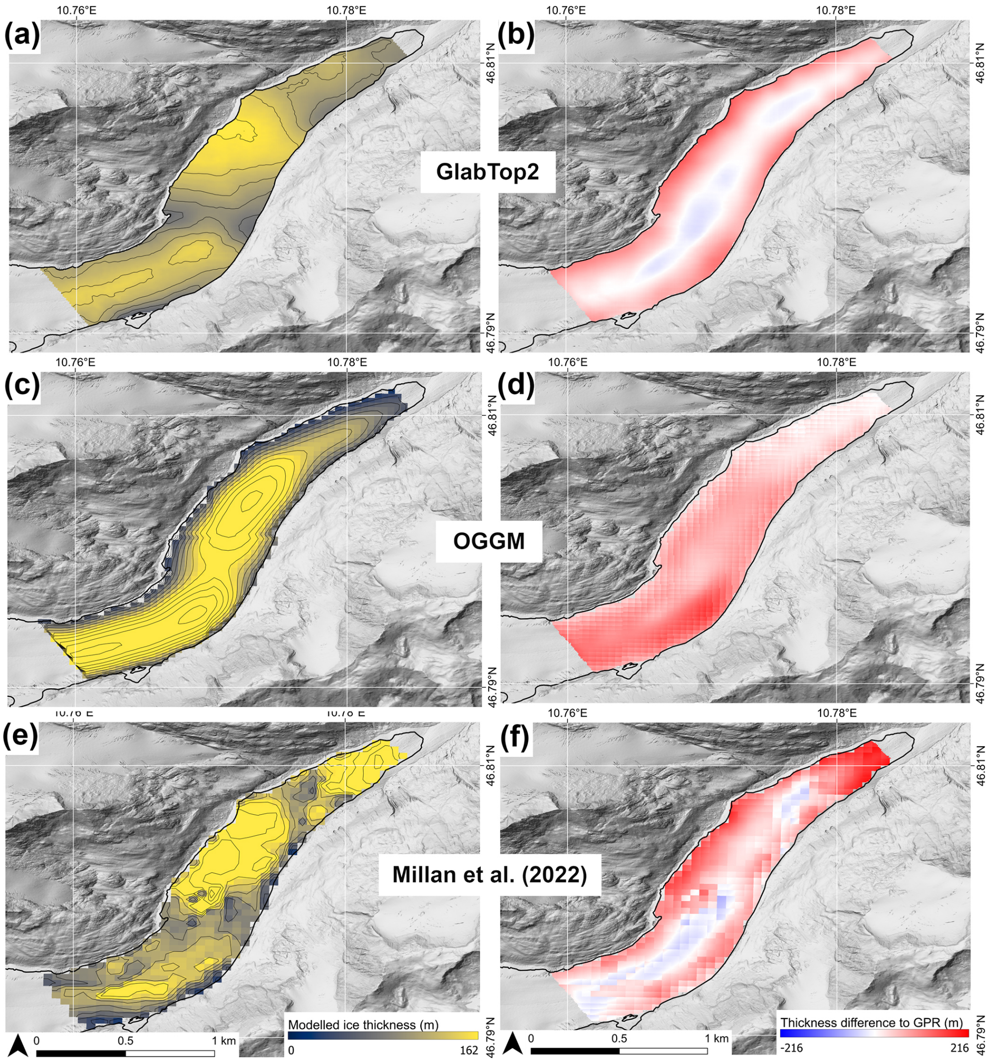

Figure 4. Modelled ice thickness (**a, c, e**; contour interval 20 m) for GlabTop2, OGGM, and Millan et al. (2022), and the corresponding difference between modelled and GPR-interpolated thickness **(b, d, f)**. Positive values in **(b)**, **(d)**, and **(f)** indicate model overestimation relative to GPR-interpolated thickness. Background hillshaded DEM data source: basemap.at (basemap.at, 2024).

vs. 40.6 m). Margin-related overestimation of the kind seen here has similarly been reported for GlabTop2 and OGGM elsewhere, attributed to interpolation procedures and simplified glacier geometry near glacier boundaries (Vergnano et al., 2025), where it was suggested that this effect would be less pronounced for elongated, valley-confined glaciers compared to wider, more complex geometries. However, despite the valley-confined geometry of HEF, margin overestimation is still present (Fig. 4), suggesting that valley confinement alone does not necessarily constrain this bias.

5.2 Sources of model biases

Although the three models differ in complexity and input data, they remain fundamentally constrained by glacier surface geometry and slope-dependent stress balance assumptions. In the absence of glacier-specific constraints on basal sliding and ice rheology, variations in ice viscosity must be balanced by the inferred thickness. Deviations from commonly assumed rheological parameters, such as a Glens' stress exponent n and rate factor A expected for temperate, water-rich ice, would reduce the thickness required to reproduce the observed velocities. Recent studies show that temperate ice may behave substantially differently from cold ice, with the stress exponents approaching $n \approx 1$ (Schohn et al., 2025) and strong weakening associated with meltwater content and strain localization (Haseloff et al., 2019). If these effects are not accounted for, deformation-based inversions tend to misattribute ice motion to increased thickness, resulting in systematic overestimation. Although local underestimation occurs in places, the net effect across the surveyed area is a positive bias. We note that these rheological ar-

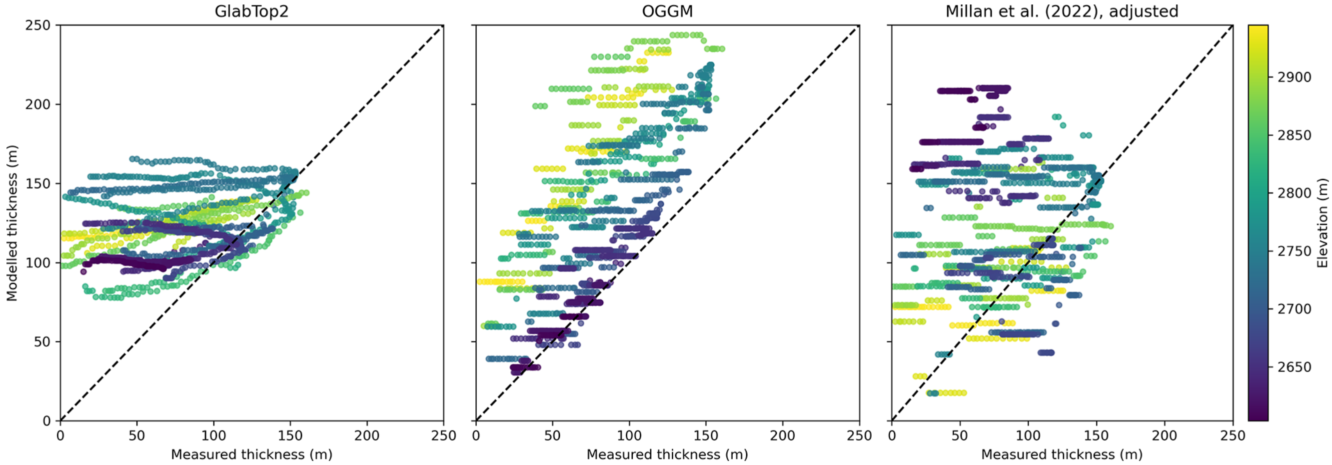

Figure 5. Comparison between measured and modelled ice thickness across the GPR-surveyed area, with points coloured by elevation. The dashed line represents 1 : 1 agreement.

guments represent possible contributing factors rather than demonstrated mechanisms. A post-hoc sensitivity analysis, i.e. tuning parameters such as the rate factor A after the true thickness is known, would not meaningfully address this, as the whole point of these models is to estimate thickness *without* prior knowledge of it. Tuning a model to match known observations on one glacier tells us little about how well it would perform elsewhere, where no thickness data exist. For models capable of forward projections, such as OGGM, the magnitude of thickness overestimation documented here suggests that projections initialised from the default model state may inherit a substantially biased ice volume, which is worth considering when interpreting projected glacier evolution – including for glaciers in the same region as HEF (Hartl et al., 2025) and at broader scales (Rounce et al., 2023; Shafeeque et al., 2026). Systematic evaluation of rheological assumptions and their effect on projection reliability across diverse glacier settings therefore remains a valuable direction for future work.

A different source of bias applies to Millan et al. (2022), whose inversion instead relies on observed surface velocities. Millan et al. report an accuracy of $\sim 10\,\mathrm{m\,yr^{-1}}$ for their satellite-derived velocity mosaics, which are provided on a 50 m grid. For HEF, however, surface velocities during the past decade are generally below $\sim 10\,\mathrm{m\,yr^{-1}}$ (Stocker-Waldhuber et al., 2024), with only localized areas possibly reaching higher values. As a result, the velocity signal is close to the uncertainty level of the velocity mosaic and provides only weak constraint on ice thickness magnitude. Under these conditions, ice thickness becomes the primary variable used to satisfy the flux continuity, leading to spatially inconsistent thickness estimates, consistent with the large bias variability observed for this model. This sensitivity to input data quality is consistent with broader model intercomparison results, where models relying on additional datasets such as surface velocity fields showed particularly high sensitivity to input data quality (Farinotti et al., 2017).The contrasting behaviour of the Millan et al. (2022) model across different glaciological settings further highlights this sensitivity. While the model overestimates thickness for the temperate, valley-confined HEF, Lamsters et al. (2024) reported substantial underestimation of up to ∼ 80–90 m along the central flowline for small, narrow, cold outlet glaciers of the Qaanaaq Ice Cap in NW Greenland.

In addition to these model-specific bias sources, we considered several potential sources of systematic error when interpreting the reported model biases. Regarding GPR-derived thickness uncertainty: as mentioned in Sect. 3.3, our cold-ice velocity assumption results in a worst-case overestimation of GPR-derived thickness of up to 7 %, meaning the true model bias is likely larger than reported here. Our bias estimates are therefore conservative. Regarding the DSM temporal offset, it is important to note that the DSM has no effect on GPR-derived ice thickness, as thickness is calculated directly from the two-way travel time between the surface and bed reflections and does not depend on any elevation reference. The DSM temporal offset is therefore solely relevant as a potential source of uncertainty in the model inputs for GlabTop2 and OGGM. The DSM–GNSS elevation differences at GPR profile locations average 2.8 m and reach a maximum of 4.9 m (Fig. A2), while maximum positive model deviations reach 146, 173, and 207 m for GlabTop2, OGGM, and Millan et al. (2022), respectively. The DSM offset therefore represents less than 3 % of the maximum overestimation and cannot account for the observed spatial pattern of thickness bias along the glacier margins. To further quantify this, we reran both GlabTop2 and OGGM with the DEM uniformly lowered by 5 m – exceeding the maximum observed DSM–GNSS difference of 4.9 m – and found that mean modelled thickness changed by less than 1 % for both GlabTop2 and

OGGM models, confirming that the DEM temporal offset has a negligible effect on modelled thickness relative to the reported biases.

5.3 Limitations

The spatial extent of GPR survey in this study must be considered when interpreting model performance. The comparison is restricted to the middle-to-lower sections of HEF, where surface slopes are relatively gentle. The steeper upper-glacier area and potential local thickness maxima were not fully covered, and bed visibility decreased towards higher elevations. Inclusion of these areas could potentially reduce the overall magnitude of overestimation, but no definitive conclusions can be drawn.

Even ground-based GPR systems, generally considered to offer the highest data quality and bedrock detection capability on temperate Alpine glaciers (Forte et al., 2019), can suffer from substantial bedrock signal loss. Across a large dataset of Swiss Alpine glaciers, Rutishauser et al. (2016) found that the bedrock interface could be identified in only 12 %–69 % of profiles, depending on the glacier. Similar limitations in bedrock visibility have been reported elsewhere, particularly where ice thickness exceeds ~ 100 m (Binder et al., 2009; Ogier et al., 2023). Although winter surveys are sometimes used to reduce attenuation from liquid water and improve bedrock detectability (Church et al., 2020), such conditions pose substantial logistical and safety challenges for ground-based GPR on Alpine glaciers due to deep snow cover and limited accessibility. In such cases, combined interpretation of GPR measurements and modelled thickness has been recommended to reduce uncertainty (Vergnano et al., 2025); however, the pronounced model biases identified in this study indicate that such approaches must be applied with caution and cannot be universally recommended.

6 Conclusions

The Hintereisferner glacier is one of 60 WGMS reference glaciers, located in the Ötztal Alps (Austria), with a long history of glaciological observations, yet lacking up-to-date ice thickness data. To address this gap, we carried out detailed low-frequency GPR measurements in August 2023 covering ~ 8.5 km of profiles and $\sim 1.3\,\mathrm{km}^2$ of the lower tongue of HEF. Despite strong signal attenuation typical for temperate Alpine glaciers, the glacier bed was identifiable in most profiles; however, bed visibility locally decreased in areas of strong signal scattering. The maximum detected ice thickness reaches ~ 160 m along the central flowline, while the mean thickness across the surveyed area is 81.1 ± 37.4 m ($\pm 1\sigma$). The derived bedrock topography reveals a well-defined U-shaped valley, consistent with the glacier geometry.

We also compared three widely applied ice thickness models (GlabTop2, OGGM and Millan et al., 2022) to our GPR data and found that the ice thickness in models is generally overestimated across the surveyed area. The mean modelled thickness ($\pm 1\sigma$) ranges from 121.6 ± 19.9 m for GlabTop2 to 131.5 ± 54.8 m for OGGM, with Millan et al. (2022), adjusted for surface lowering between 2018 and 2023, at 127.5 ± 44.9 m. The corresponding mean errors ($\pm 1\sigma$) are 40.6 ± 35.6 m for GlabTop2, 48.6 ± 37.5 m for OGGM, and 46.0 ± 57.0 m for Millan et al. (2022). Among the three, only OGGM reproduces the correct spatial pattern of ice thickness distribution, though this does not translate into accurate thickness magnitudes. Our results highlight persistent limitations of both geometry-based and velocity-informed models when applied to small, temperate valley glaciers, where ice rheology and basal conditions are difficult to constrain with default model configurations. These findings underscore the need for continued field-based ice thickness measurements across a wider range of glacier types and settings, to systematically evaluate model performance under real-world conditions where thickness data are typically unavailable, particularly given their role in projecting future glacier evolution.

Appendix A: Field photographs and supporting data

Figure A1 shows field photographs from our GPR survey conducted on Hintereisferner in August 2023, illustrating the survey conditions and equipment setup. The survey was carried out on a snow-free glacier surface and mostly under clear weather conditions.

During the GPR survey, we recorded precise GNSS positions at the start and end points of each profile using an Emlid Reach RS2 receiver, yielding 193 measurement points spaced approximately 50 m apart along the profiles. Figure A2 shows the elevation differences between these GNSS-derived heights and the corresponding values extracted from the 2022 DSM at the same locations. These differences reflect surface lowering between the DSM acquisition date (September 2022) and the GPR survey date (August 2023) and were used to assess the potential influence of the DSM temporal offset on modelled ice thickness, as discussed in Sect. 4.2.

Figure A1. Field photographs from the GPR survey on Hintereisferner, Ötztal Alps, Austria, August 2023. **(a)** Aerial view of the GPR survey area on the lower glacier tongue, showing light snow cover following a snowfall (2 August 2023). **(b)** GPR survey in progress on snow-free glacier ice, showing two GPR operators carrying the Zond-xLF GPR system along a transverse profile (3 August 2023). **(c)** Moulin on the glacier surface, illustrating the crevassed and hydrologically active character of the lower tongue (5 August 2023).

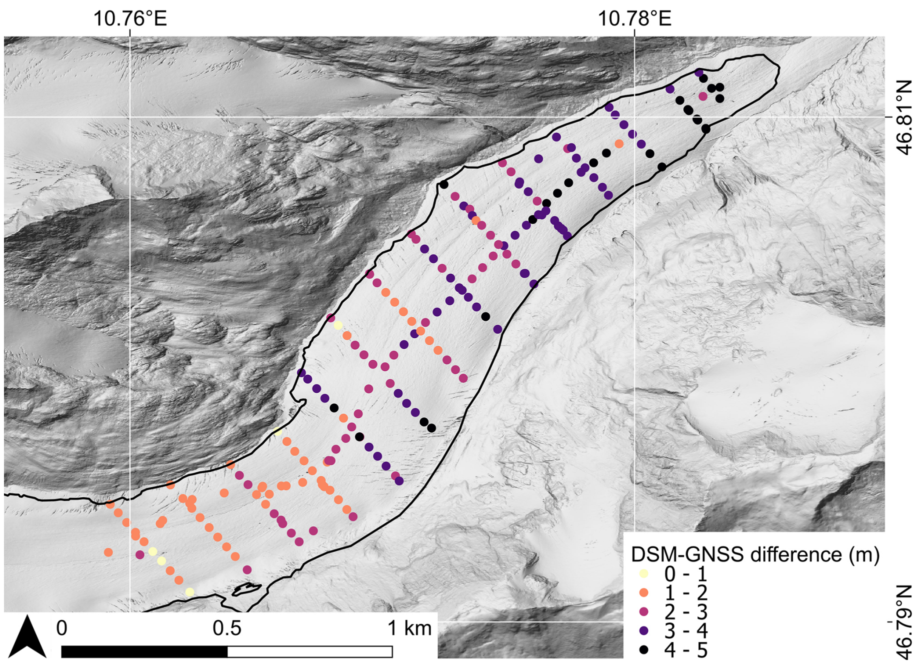

Figure A2. Spatial distribution of elevation differences between the 2022 DSM and GNSS-surveyed points ($n = 193$) collected during the August 2023 GPR survey. Differences range from 0.4–4.9 (mean 2.8 ± 0.9 m, $\pm 1\sigma$). Background hillshaded DEM data source: basemap.at (basemap.at, 2024).

Code and data availability. All the GPR data, derived bedrock picks, and model configuration and parameter files used in this study are available via a Zenodo repository at: https://doi.org/10.5281/zenodo.21114612 (Švinka et al., 2026). The repository is organized into five subfolders, each accompanied by a README file, describing the contents and workflow steps.

A DSM was obtained from ALS campaign conducted on 23 September 2022, and provided by Rainer Prinz (Department of Atmospheric and Cryospheric Sciences, University of Innsbruck, Austria). The glacier outline was derived from Pléiades satellite images that were acquired on 21 August 2022 (Pléiades © CNES 2022, Distribution Airbus D&S).

Ice thickness modelling was performed using open-source models. The GlabTop2-Py model is available at https://glabtop2-py.readthedocs.io/en/latest/index.html (last access: 10 November 2025), and the OGGM model is available at https://docs.oggm.org/en/stable/ (last access: 10 November 2025). In addition, ice thickness estimates from the global ice thickness model of Millan et al. (2022) were used. The thickness product was obtained from the THEIA data centre at https://www.sedoo.fr/theia-publication-products/?uuid=55acbdd5-3982-4eac-89b2-46703557938c (last access: 10 November 2025). Glaciological mass balance data for Hintereisferner, used to derive the elevation-band temporal correction applied to the Millan et al. (2022) thickness estimates, were obtained from the WGMS Fluctuations of Glaciers Database (WGMS, 2026), https://doi.org/10.5904/wgms-fog-2026-02-10.

Author contributions. Conceptualization: LŠ, KL, JK. Data Acquisition: LŠ, KL, PD. Data processing: LŠ, JJ. Data analyses: LŠ, KL, JK. Writing: LŠ, KL, JK. Visualization: LŠ.

Competing interests. The contact author has declared that none of the authors has any competing interests.

Disclaimer. Publisher's note: Copernicus Publications remains neutral with regard to jurisdictional claims made in the text, published maps, institutional affiliations, or any other geographical representation in this paper. The authors bear the ultimate responsibility for providing appropriate place names. Views expressed in the text are those of the authors and do not necessarily reflect the views of the publisher.

Acknowledgements. Station Hintereis manager Rainer Prinz is warmly acknowledged for all logistical help and especially fast transportation to the base via helicopter.

Financial support. The research leading to these results has received Transnational Access from the European Union's Horizon 2020 project INTERACT, under grant agreement no. 871120.

Review statement. This paper was edited by Adam Booth and reviewed by Adriano Ribolini and two anonymous referees.

References

Abermann, J., Lambrecht, A., Fischer, A., and Kuhn, M.: Quantifying changes and trends in glacier area and volume in the Austrian Ötztal Alps (1969–1997–2006), The Cryosphere, 3, 205–215, https://doi.org/10.5194/tc-3-205-2009, 2009.

basemap.at: Geoland Basemap Gelände (hillshade), https://basemap.at/en/gelaende/ (last access: 30 July 2024), 2024.

Binder, D., Brückl, E., Roch, K. H., Behm, M., Schöner, W., and Hynek, B.: Determination of total ice volume and ice-thickness distribution of two glaciers in the Hohe Tauern region, Eastern Alps, from GPR data, Ann. Glaciol., 50, 71–79, https://doi.org/10.3189/172756409789097522, 2009.

Bogorodsky, V. V., Bentley, C. R., and Gudmandsen, P.: Radioglaciology, Springer Science & Business Media, ISBN 978-94-009-5275-1, 2012.

Bradford, J. H. and Harper, J. T.: Wave field migration as a tool for estimating spatially continuous radar velocity and water content in glaciers, Geophys. Res. Lett., 32, 2004GL021770, https://doi.org/10.1029/2004GL021770, 2005.

Chambers, J. R., Smith, M. W., Smith, T., Sailer, R., Quincey, D. J., Carrivick, J. L., Nicholson, L., Mertes, J., Stiperski, I., and James, M. R.: Correcting for Systematic Underestimation of Topographic Glacier Aerodynamic Roughness Values From Hintereisferner, Austria, Front. Earth Sci., 9, 691195, https://doi.org/10.3389/feart.2021.691195, 2021.

Chen, W., Yao, T., Zhang, G., Li, F., Zheng, G., Zhou, Y., and Xu, F.: Towards ice-thickness inversion: an evaluation of global digital elevation models (DEMs) in the glacierized Tibetan Plateau, The Cryosphere, 16, 197–218, https://doi.org/10.5194/tc-16-197-2022, 2022.

Church, G., Grab, M., Schmelzbach, C., Bauder, A., and Maurer, H.: Monitoring the seasonal changes of an englacial conduit network using repeated ground-penetrating radar measurements, The Cryosphere, 14, 3269–3286, https://doi.org/10.5194/tc-14-3269-2020, 2020.

Cook, S. J., Jouvet, G., Millan, R., Rabatel, A., Zekollari, H., and Dussaillant, I.: Committed Ice Loss in the European Alps Until 2050 Using a Deep-Learning-Aided 3D Ice-Flow Model With Data Assimilation, Geophys. Res. Lett., 50, e2023GL105029, https://doi.org/10.1029/2023GL105029, 2023.

Delf, R., Bingham, R. G., Curtis, A., Singh, S., Giannopoulos, A., Schwarz, B., and Borstad, C. P.: Reanalysis of Polythermal Glacier Thermal Structure Using Radar Diffraction Focusing, J. Geophys. Res.-Earth, 127, https://doi.org/10.1029/2021JF006382, 2022.

Farinotti, D., Huss, M., Bauder, A., Funk, M., and Truffer, M.: A method to estimate the ice volume and ice-thickness distribution of alpine glaciers, J. Glaciol., 55, 422–430, https://doi.org/10.3189/002214309788816759, 2009.

Farinotti, D., Brinkerhoff, D. J., Clarke, G. K. C., Fürst, J. J., Frey, H., Gantayat, P., Gillet-Chaulet, F., Girard, C., Huss, M., Leclercq, P. W., Linsbauer, A., Machguth, H., Martin, C., Maussion, F., Morlighem, M., Mosbeux, C., Pandit, A., Portmann, A., Rabatel, A., Ramsankaran, R., Reerink, T. J., Sanchez, O., Stentoft, P. A., Singh Kumari, S., van Pelt, W. J. J., Anderson, B., Benham, T., Binder, D., Dowdeswell, J. A., Fischer, A., Helfricht, K., Kutuzov, S., Lavrentiev, I., McNabb, R., Gudmundsson, G. H., Li, H., and Andreassen, L. M.: How accurate are estimates of glacier ice thickness? Results from ITMIX, the Ice Thickness Models Intercomparison eXperiment, The Cryosphere, 11, 949–970, https://doi.org/10.5194/tc-11-949-2017, 2017.

Fischer, A.: Glaciers and climate change: Interpretation of 50 years of direct mass balance of Hintereisferner, Global Planet. Change, 71, 13–26, https://doi.org/10.1016/j.gloplacha.2009.11.014, 2010.

Fischer, A. and Kuhn, M.: Ground-penetrating radar measurements of 64 Austrian glaciers between 1995 and 2010, Ann. Glaciol., 54, 179–188, https://doi.org/10.3189/2013AoG64A108, 2013.

Fischer, A., Markl, G., and Kuhn, M.: Glacier Mass Balance of Hintereisferner, Oetztal Alps, Austria, from 1952/53–2010/11, World Data Center for Climate (WDCC) at DKRZ, https://doi.org/10.1594/WDCC/MB_HEF_1953-2011, 2012.

Fischer, A., Seiser, B., Stocker Waldhuber, M., Mitterer, C., and Abermann, J.: Tracing glacier changes in Austria from the Little Ice Age to the present using a lidar-based high-resolution glacier inventory in Austria, The Cryosphere, 9, 753–766, https://doi.org/10.5194/tc-9-753-2015, 2015.

Forte, E., Bondini, M. B., Bortoletto, A., Dossi, M., and Colucci, R. R.: Pros and Cons in Helicopter-Borne GPR Data Acquisition on Rugged Mountainous Areas: Critical Analysis and Practical Guidelines, Pure Appl. Geophys., 176, 4533–4554, https://doi.org/10.1007/s00024-019-02196-2, 2019.

Forte, E., Gutgesell, P., Securo, A., Marcer, M., Citterio, M., Machguth, H., and Colucci, R. R.: Comparing GPR with ice thickness and thermal models: Insights from two polythermal glaciers in West Greenland, J. Glaciol., 71, e97, https://doi.org/10.1017/jog.2025.10067, 2025.

Förtsch, O. and Vidal, H.: Glaziologische und glazialgeologische Ergebnisse seismischer Messungen auf Gletschern der Ötztaler Alpen 1953/54, Zeitschrift für Gletscherkunde und Glazialgeologie, 3, 145–169, 1956.

Frey, H., Machguth, H., Huss, M., Huggel, C., Bajracharya, S., Bolch, T., Kulkarni, A., Linsbauer, A., Salzmann, N., and Stoffel, M.: Estimating the volume of glaciers in the Himalayan–Karakoram region using different methods, The Cryosphere, 8, 2313–2333, https://doi.org/10.5194/tc-8-2313-2014, 2014.

Galos, S., Klug, C., and Dinale, R.: Short Communication: The 2023 Glacier Inventory for South Tyrol in Context of the Inventories 1997, 2005 and 2017, Geogr. Fis. Din. Quat., 47, 381–388, https://doi.org/10.4454/5agvnb15, 2025.

Gusmeroli, A., Jansson, P., Pettersson, R., and Murray, T.: Twenty years of cold surface layer thinning at Storglaciären, sub-Arctic Sweden, 1989–2009, J. Glaciol., 58, 3–10, https://doi.org/10.3189/2012JoG11J018, 2012.

Hartl, L., Schmitt, P., Schuster, L., Helfricht, K., Abermann, J., and Maussion, F.: Recent observations and glacier modeling point towards near-complete glacier loss in western Austria (Ötztal and Stubai mountain range) if 1.5 °C is not met, The Cryosphere, 19, 1431–1452, https://doi.org/10.5194/tc-19-1431-2025, 2025.

Haseloff, M., Hewitt, I. J., and Katz, R. F.: Englacial Pore Water Localizes Shear in Temperate Ice Stream Margins, J. Geophys. Res.-Earth, 124, 2521–2541, https://doi.org/10.1029/2019JF005399, 2019.

Helfricht, K., Kuhn, M., Keuschnig, M., and Heilig, A.: Lidar snow cover studies on glaciers in the Ötztal Alps (Austria): comparison with snow depths calculated from GPR measurements, The Cryosphere, 8, 41–57, https://doi.org/10.5194/tc-8-41-2014, 2014.

Hugonnet, R., McNabb, R., Berthier, E., Menounos, B., Nuth, C., Girod, L., Farinotti, D., Huss, M., Dussaillant, I., Brun, F., and Kääb, A.: Accelerated global glacier mass loss in the early twenty-first century, Nature, 592, 726–731, https://doi.org/10.1038/s41586-021-03436-z, 2021.

Jania, J., Mochnacki, D., and Gadek, B.: The thermal structure of Hansbreen, a tidewater glacier in southern Spitsbergen, Svalbard, Polar Res., 15, 53–66, 1996.

Jol, H. M.: Ground penetrating radar theory and applications, Elsevier, ISBN 978-0-444-53348-7, 2008.

Karušs, J., Lamsters, K., Chernov, A., Krievāns, M., and Ješkins, J.: Subglacial topography and thickness of ice caps on the Argentine Islands, Antarct. Sci., 31, 332–344, https://doi.org/10.1017/S0954102019000452, 2019.

Karušs, J., Lamsters, K., Sobota, I., Ješkins, J., Džeriņš, P., and Hodson, A.: Drainage system and thermal structure of a High Arctic polythermal glacier: Waldemarbreen, western Svalbard, J. Glaciol., 68, 591–604, https://doi.org/10.1017/jog.2021.125, 2022.

Klug, C., Bollmann, E., Galos, S. P., Nicholson, L., Prinz, R., Rieg, L., Sailer, R., Stötter, J., and Kaser, G.: Geodetic reanalysis of annual glaciological mass balances (2001–2011) of Hintereisferner, Austria, The Cryosphere, 12, 833–849, https://doi.org/10.5194/tc-12-833-2018, 2018.

Lamsters, K., Karušs, J., Krievāns, M., and Ješkins, J.: High-resolution orthophoto map and digital surface models of the largest Argentine Islands (the Antarctic) from unmanned aerial vehicle photogrammetry, J. Maps, 16, 335–347, https://doi.org/10.1080/17445647.2020.1748130, 2020a.

Lamsters, K., Karušs, J., Krievāns, M., and Ješkins, J.: The thermal structure, subglacial topography and surface structures of the NE outlet of Eyjabakkajökull, east Iceland, Polar Sci., 26, 100566, https://doi.org/10.1016/j.polar.2020.100566, 2020b.

Lamsters, K., Karušs, J., Ješkins, J., Džeriņš, P., Ukai, S., and Sugiyama, S.: Geometry and thermal regime of the southern outlet glaciers of Qaanaaq Ice Cap, NW Greenland, Earth Surf. Proc. Land., 49, 4275–4288, https://doi.org/10.1002/esp.5966, 2024.

Linsbauer, A., Huss, M., Hodel, E., Bauder, A., and Barandun, M.: Vanished glaciers of the Swiss Alps: An inventory-based assessment from 1973 to 2016, Ann. Glaciol., 66, e33, https://doi.org/10.1017/aog.2025.10031, 2025.

Maussion, F., Butenko, A., Champollion, N., Dusch, M., Eis, J., Fourteau, K., Gregor, P., Jarosch, A. H., Landmann, J., Oesterle, F., Recinos, B., Rothenpieler, T., Vlug, A., Wild, C. T., and Marzeion, B.: The Open Global Glacier Model (OGGM) v1.1, Geosci. Model Dev., 12, 909–931, https://doi.org/10.5194/gmd-12-909-2019, 2019.

Millan, R., Mouginot, J., Rabatel, A., and Morlighem, M.: Ice velocity and thickness of the world's glaciers, Nat. Geosci., 15, 124–129, https://doi.org/10.1038/s41561-021-00885-z, 2022.

Mott, R., Stiperski, I., and Nicholson, L.: Spatio-temporal flow variations driving heat exchange processes at a mountain glacier, The

Cryosphere, 14, 4699–4718, https://doi.org/10.5194/tc-14-4699-2020, 2020.

Murray, T., Stuart, G. W., Fry, M., Gamble, N. H., and Crabtree, M. D.: Englacial water distribution in a temperate glacier from surface and borehole radar velocity analysis, J. Glaciol., 46, 389–398, https://doi.org/10.3189/172756500781833188, 2000.

Murray, T., Booth, A., and Rippin, D. M.: Water-Content of Glacier-Ice: Limitations on Estimates from Velocity Analysis of Surface Ground-Penetrating Radar Surveys, J. Environ. Eng. Geoph., 12, 87–99, https://doi.org/10.2113/jeeg12.1.87, 2007.

Navarro, F. and Eisen, O. (Eds.): 11 Ground-penetrating radar in glaciological applications, in: Remote sensing of glaciers: Techniques for topographic, spatial and thematic mapping of glaciers, CRC Press, 195–229, https://doi.org/10.1201/b10155-12, 2009.

Nicholson, L., Stiperski, I., Nitti, G., Prinz, R., Georgi, A., Groos, A. R., Shaw, T. E., Sauter, T., Haugeneder, M., Mott, R., Sicart, J.-E., Brock, B. W., Albers, R., Allegri, B., Barral, H., Biron, R., Charrondiere, C., Coulaud, C., Fischer, A., Reynolds, D., Richter, N., Schroeder, M., Vettori, P., Voordendag, A., and Wydra, C.: The Second Hintereisferner Experiment (HEFEX II): Initial Insights into Boundary Layer Structure and Surface–Atmosphere Exchange Processes from Intensive Observations at a Valley Glacier, B. Am. Meteorol. Soc., 106, E2143–E2169, https://doi.org/10.1175/BAMS-D-24-0010.1, 2025.

Ogier, C., Van Manen, D.-J., Maurer, H., Räss, L., Hertrich, M., Bauder, A., and Farinotti, D.: Ground penetrating radar in temperate ice: englacial water inclusions as limiting factor for data interpretation, J. Glaciol., 1–12, https://doi.org/10.1017/jog.2023.68, 2023.

Pellikka, P. and Rees, W. G.: Remote sensing of glaciers: techniques for topographic, spatial and thematic mapping of glaciers, CRC Press, ISBN 978-0-415-40166-1, 2009.

Pelto, B. M., Maussion, F., Menounos, B., Radić, V., and Zeuner, M.: Bias-corrected estimates of glacier thickness in the Columbia River Basin, Canada, J. Glaciol., 66, 1051–1063, https://doi.org/10.1017/jog.2020.75, 2020.

Raper, S. C. B., Brown, O., and Braithwaite, R. J.: A geometric glacier model for sea-level change calculations, J. Glaciol., 46, 357–368, https://doi.org/10.3189/172756500781833034, 2000.

Rippin, D. M., Carrivick, J. L., and Williams, C.: Evidence towards a thermal lag in the response of Kårsaglaciären, northern Sweden, to climate change, J. Glaciol., 57, 895–903, https://doi.org/10.3189/002214311798043672, 2011.

Robin, G. D. Q.: Velocity of radio waves in ice by means of a bore-hole interferometric technique, J. Glaciol., 15, 151–159, https://doi.org/10.3189/S0022143000034341, 1975.

Rounce, D. R., Hock, R., Maussion, F., Hugonnet, R., Kochtitzky, W., Huss, M., Berthier, E., Brinkerhoff, D., Compagno, L., Copland, L., Farinotti, D., Menounos, B., and McNabb, R. W.: Global glacier change in the 21st century: Every increase in temperature matters, Science, 379, 78–83, https://doi.org/10.1126/science.abo1324, 2023.

Rutishauser, A., Maurer, H., and Bauder, A.: Helicopter-borne ground-penetrating radar investigations on temperate alpine glaciers: A comparison of different systems and their abilities for bedrock mapping, Geophysics, 81, WA119–WA129, https://doi.org/10.1190/GEO2015-0144.1, 2016.

Santin, I., Colucci, R. R., Žebre, M., Pavan, M., Cagnati, A., and Forte, E.: Recent evolution of Marmolada glacier (Dolomites, Italy) by means of ground and airborne GPR surveys, Remote Sens. Environ., 235, 111442, https://doi.org/10.1016/j.rse.2019.111442, 2019.

Schohn, C. M., Iverson, N. R., Zoet, L. K., Fowler, J. R., and Morgan-Witts, N.: Linear-viscous flow of temperate ice, Science, 387, 182–185, https://doi.org/10.1126/science.adp7708, 2025.

Schroeder, D. M., Bingham, R. G., Blankenship, D. D., Christianson, K., Eisen, O., Flowers, G. E., Karlsson, N. B., Koutnik, M. R., Paden, J. D., and Siegert, M. J.: Five decades of radioglaciology, Ann. Glaciol., 61, 1–13, https://doi.org/10.1017/aog.2020.11, 2020.

Sevestre, H., Benn, D. I., Hulton, N. R. J., and Bælum, K.: Thermal structure of Svalbard glaciers and implications for thermal switch models of glacier surging, J. Geophys. Res.-Earth, 120, 2220–2236, https://doi.org/10.1002/2015JF003517, 2015.

Shafeeque, M., Malles, J.-H., Vlug, A., Möller, M., and Marzeion, B.: Projecting the response of Greenland's peripheral glaciers to future climate change: glacier losses, sea level impact, freshwater contributions, and peak water timing, The Cryosphere, 20, 875–903, https://doi.org/10.5194/tc-20-875-2026, 2026.

Span, N., Fischer, A., Kuhn, M., Massimo, M., and Butschek, M.: Radarmessungen der Eisdicke österreichischer Gletscher, Band I: Messungen 1995 bis 1998, Österreichische Beiträge zur Meteorologie und Geophysik, Zentralanstalt für Meteorologie und Geodynamik (ZAMG), Vienna, 33, 145 pp., 2005.

Stocker-Waldhuber, M., Fischer, A., Helfricht, K., Kuhn, M., Schneider, H., and Span, N.: Glacier surface velocities of Hintereisferner, 2022/2023, https://doi.org/10.1594/PANGAEA.970134, 2024.

Strasser, U., Marke, T., Braun, L., Escher-Vetter, H., Juen, I., Kuhn, M., Maussion, F., Mayer, C., Nicholson, L., Niedertscheider, K., Sailer, R., Stötter, J., Weber, M., and Kaser, G.: The Rofental: a high Alpine research basin (1890–3770 m a.s.l.) in the Ötztal Alps (Austria) with over 150 years of hydrometeorological and glaciological observations, Earth Syst. Sci. Data, 10, 151–171, https://doi.org/10.5194/essd-10-151-2018, 2018.

Švinka, L., Karušs, J., and Lamsters, K.: Ice thickness inversion assessment: A comparison study for Waldemarbreen and Irenebreen glaciers, Svalbard, Polar Sci., 43, 101167, https://doi.org/10.1016/j.polar.2025.101167, 2025.

Švinka, L., Lamsters, K., Karušs, J., Džeriņš, P., and Ješkins, J.: Supplementary materials for the publication "GPR-derived ice thickness of the temperate Hintereisferner glacier (Austrian Alps): evaluation of thickness models", Zenodo [data set] and [code], https://doi.org/10.5281/zenodo.21114612, 2026.

The GlaMBIE Team, Zemp, M., Jakob, L., Dussaillant, I., Nussbaumer, S. U., Gourmelen, N., Dubber, S., A, G., Abdullahi, S., Andreassen, L. M., Berthier, E., Bhattacharya, A., Blazquez, A., Boehm Vock, L. F., Bolch, T., Box, J., Braun, M. H., Brun, F., Cicero, E., Colgan, W., Eckert, N., Farinotti, D., Florentine, C., Floricioiu, D., Gardner, A., Harig, C., Hassan, J., Hugonnet, R., Huss, M., Jóhannesson, T., Liang, C.-C. A., Ke, C.-Q., Khan, S. A., King, O., Kneib, M., Krieger, L., Maussion, F., Mattea, E., McNabb, R., Menounos, B., Miles, E., Moholdt, G., Nilsson, J., Pálsson, F., Pfeffer, J., Piermattei, L., Plummer, S., Richter, A., Sasgen, I., Schuster, L., Seehaus, T., Shen, X., Sommer, C., Sutterley, T., Treichler, D., Velicogna, I., Wouters, B., Zekollari, H., and Zheng, W.: Community estimate of global glacier mass changes from 2000 to 2023, Nature, 639, 382–388, https://doi.org/10.1038/s41586-024-08545-z, 2025.

Van Tricht, L., Zekollari, H., Huss, M., Rounce, D. R., Schuster, L., Aguayo, R., Schmitt, P., Maussion, F., Tober, B., and Farinotti, D.: Peak glacier extinction in the mid-twenty-first century, Nat. Clim. Change, 16, 143–147, https://doi.org/10.1038/s41558-025-02513-9, 2026.

Vergnano, A., Franco, D., and Godio, A.: Integrating GPR and ice-thickness models for improved bedrock detection: the case study of Rutor temperate glacier, The Cryosphere, 19, 6965–6988, https://doi.org/10.5194/tc-19-6965-2025, 2025.

Voordendag, A., Prinz, R., Schuster, L., and Kaser, G.: Brief communication: The Glacier Loss Day as an indicator of a record-breaking negative glacier mass balance in 2022, The Cryosphere, 17, 3661–3665, https://doi.org/10.5194/tc-17-3661-2023, 2023a.

Voordendag, A., Goger, B., Klug, C., Prinz, R., Rutzinger, M., Sauter, T., and Kaser, G.: Uncertainty assessment of a permanent long-range terrestrial laser scanning system for the quantification of snow dynamics on Hintereisferner (Austria), Front. Earth Sci., 11, 1085416, https://doi.org/10.3389/feart.2023.1085416, 2023b.

Watts, R. D. and England, A. W.: Radio-echo Sounding of Temperate Glaciers: Ice Properties and Sounder Design Criteria, J. Glaciol., 17, 39–48, https://doi.org/10.3189/S0022143000030707, 1976.

WGMS: Fluctuations of Glaciers (FoG) Database (2026-02-10), WGMS [data set], https://doi.org/10.5904/WGMS-FOG-2026-02-10, 2026.

Zekollari, H., Huss, M., and Farinotti, D.: Modelling the future evolution of glaciers in the European Alps under the EURO-CORDEX RCM ensemble, The Cryosphere, 13, 1125–1146, https://doi.org/10.5194/tc-13-1125-2019, 2019.

Zekollari, H., Huss, M., Schuster, L., Maussion, F., Rounce, D. R., Aguayo, R., Champollion, N., Compagno, L., Hugonnet, R., Marzeion, B., Mojtabavi, S., and Farinotti, D.: Twenty-first century global glacier evolution under CMIP6 scenarios and the role of glacier-specific observations, The Cryosphere, 18, 5045–5066, https://doi.org/10.5194/tc-18-5045-2024, 2024.

Zemp, M., Huss, M., Thibert, E., Eckert, N., McNabb, R., Huber, J., Barandun, M., Machguth, H., Nussbaumer, S. U., Gärtner-Roer, I., Thomson, L., Paul, F., Maussion, F., Kutuzov, S., and Cogley, J. G.: Global glacier mass changes and their contributions to sea-level rise from 1961 to 2016, Nature, 568, 382–386, https://doi.org/10.1038/s41586-019-1071-0, 2019.